



Final Draft of the original manuscript

Xia, D.; Zhang, J.; Chen, X.; Huang, G.; Jiang, B.; Tang, A.; Gavras, S.;
Huang, Y.; Hort, N.; Pan, F.:

**Effect of biaxial compressive stress state on the microstructure
evolution and deformation compatibility of rolled sheet Mg
alloy AZ31 at room temperature.**

In: Materials Science and Engineering: A. Vol. 789 (2020) 139599.

First published online by Elsevier: 27.05.2020

<https://dx.doi.org/10.1016/j.msea.2020.139599>

Effect of biaxial compressive stress state on the microstructure evolution and deformation compatibility of rolled sheet Mg alloy AZ31 at room temperature

Dabiao Xia ^{a,b,c,d}, Junlei Zhang ^{a,c}, Xiang Chen ^{a,c}, Guangsheng Huang ^{a,c,*}, Bin Jiang ^{a,c,*}, Aitao Tang ^{a,c}, Sarkis Gavras ^d, Yuanding Huang ^d, Norbert Hort ^d, Fusheng Pan ^{a,c}

^a State Key Laboratory of Mechanical Transmission, College of Materials Science and Engineering, Chongqing University, Chongqing 400044, China

^b The Center of New Energy Materials and Manufacturing, Jihua Laboratory, Foshan, 528000, China

^c National Engineering Research Center for Magnesium Alloys, Chongqing University, Chongqing 400044, China

^d MagIC-Magnesium Innovation Centre, Helmholtz-Zentrum Geesthacht, Max-Planck-Str. 1, 21502 Geesthacht, Germany

Abstract

Mg alloys usually deform under complex biaxial compressive stress states (e.g. during drawing, forging and extrusion). In order to better understand how the biaxial compressive stress state influences the evolution of the microstructure and the deformation compatibility, the uniaxial and biaxial compression tests of AZ31 rolled sheets were performed at room temperature. The new self-developed biaxial compression devices offered a possibility to obtain the evolution of the microstructures by *in situ* measurements via electron backscatter diffraction. The analysis of geometrically necessary dislocation and the simulation based on the visco-plastic self-consistent method were used to examine the microscopic behaviors in the sheets during the uniaxial and biaxial compression tests. The results indicated that the reorientation of the texture during the biaxial compression was different from that during the uniaxial compression. The simulated results based on the visco-plastic self-consistent model suggested that the equivalent yield

* Corresponding author: College of Materials Science and Engineering, Chongqing University, Chongqing 400044, China.

E-mail address: gshuang@cqu.edu.cn (G.S. Huang), binjiang@cqu.edu.cn (B. Jiang).

strength under a biaxial compressive stress state was lower than that under a uniaxial stress state. This was due to the higher relative activity of extension twins under biaxial compressive stress state. This also led to a lower geometrically necessary dislocation density in the biaxial compressed sample. The geometrically necessary dislocations were also more homogeneously distributed with a biaxial compressive stress state. The analysis of the activation of all the deformation mechanisms proved that the appearance of extension twinning variants limited the activation of prismatic slip during the uniaxial compression while promoting prismatic slip during the biaxial compression. This changeable interaction between extension twinning and prismatic slip combining with the lower geometrically necessary dislocations, the lower flow stress inferred that the application of the biaxial compressive stress state during processing at room temperature was a way to improve the deformability of Mg alloys.

Keywords: stress state; visco-plastic self-consistent model; global Schmid factor; geometrically necessary dislocation; deformation compatibility

1. Introduction

As a result of the increasing demand of lightweight materials in the transportation industry, Mg alloys with excellent strength-to-weight ratio have gained great technological importance [1-4]. To broaden the application of Mg alloys and improve the production efficiency, a more accurate of the responses of Mg alloys under different stress states is necessary for traditional modeling processes (e.g. forging, extrusion, stamping, rolling and bending) [5-8]. However, hexagonal close packed (HCP) metals such as Mg alloys, have a very pronounced strength differential effect and deformation anisotropy [9-13]. According to the literature, the strength differential effect, mainly performing as higher tensile strength than compressive strength, was a consequence of the directionality of twinning in Mg alloys [14, 15]. The anisotropy mainly results from the strong texture, which may lead to a lower strength in the rolling direction (RD) than the transverse direction (TD) [16, 17]. Hence, the mechanical properties of HCP metals are highly asymmetric and anisotropic, especially for Mg alloy rolled sheets [18-20]. Therefore, it is difficult to predict the mechanical response of Mg alloys under different stress states.

Microstructural changes are, in general, a key component to changes in mechanical properties. As such, numerous studies related to the deformation mechanisms in Mg alloys under different

load conditions were published in recent years. For instance, Mg alloys with HCP crystalline structure have a reduced number of available slip systems compared to cubic lattices at room temperature [21]. The deformation modes in Mg alloys mainly contained basal $\langle a \rangle$, prismatic $\langle a \rangle$, pyramidal $\langle a \rangle$, pyramidal $\langle a+c \rangle$ slip systems, extension twinning (ET) and contraction twinning. Via electron backscatter diffraction (EBSD), *in situ* experiments and visco-plastic self-consistent (VPSC) simulations, basal $\langle a \rangle$, pyramidal $\langle a+c \rangle$ slip systems and ET were shown to be the main mechanisms to satisfy the ductility of Mg at low temperatures [22-27]. These modes also have different polarities, activation barriers, cross hardening effects and critical resolved shear stresses (CRSS) for activation [28-31].

However, most of these studies were only under simple load conditions such as uniaxial tension or compression. It is difficult to determine the individual responses of the above mechanisms and their contributions to the plastic flow under complicated stress states e.g. biaxial compressive or biaxial shearing stress state. One of the main reasons for this is the difficulty in designing the testers and specimens used to obtain the mechanical properties under different stress states [32-35]. Steglich *et al.* [36] studied the deformation behavior of AZ31 under biaxial tensile stress state using cruciform specimen tests and bulge tests. The results revealed an increased tangent modulus of Mg alloys under biaxial tensile stress state. In the previous work published, the different evolutions of microstructures in Mg alloy rolled sheets under uniaxial tensile and biaxial tensile stress states using special biaxial tension devices were investigated [37]. The results indicated that the appearance of extension twins had no influence on the activation of prismatic and pyramidal $\langle a \rangle$ slips during the uniaxial tension while limiting their activation during the biaxial tension. Additionally, the distribution of the microscopic strain under a biaxial tensile stress state was more inhomogeneous than that under a uniaxial tensile stress state [38].

However, studies regarding the influences of complex compressive stress states on the microscopic behaviors and the deformation compatibility in Mg alloys are rare. Jia *et al.* [39] investigated the mechanical properties of AZ31 Mg alloy sheets under compressive loading conditions using a set of special specimens. Based on the results, an all-encompassing understanding of strength, plastic flow and fracture properties of Mg alloy sheets under different stress states was obtained. Zhang *et al.* [40] reported that twin pairs could form due to associated or isolated nucleation mechanisms under biaxial compressive stress state. However, a deeper

understanding of the microstructure evolution and the deformation compatibility between the deformation mechanisms under complex compressive stress states is still needed.

In this paper, the mechanical properties were examined via typical uniaxial tension and compression tests along RD and TD. Then the microstructure evolution of AZ31 rolled sheets under a uniaxial compressive stress state (UC) and a biaxial compressive stress state (BC) were systemically studied. By employing self-developed devices used for the biaxial compression, the *in situ* EBSD measurements were used to investigate the changes of the microstructures with increasing strain. In combination with VPSC simulations and the geometrically necessary dislocation (GND) analysis, the influences of BC on the evolution of the microstructures and the interactions between the deformation mechanisms are systemically investigated.

2. Materials and methods

The material used for the *in situ* compression tests was a commercial AZ31 hot-rolled sheet with 15 mm thickness from Yinguang Magnesium Industry Group Co., LTD. The composition of this material is measured using X-ray Fluorescence Spectrometer-1800 and summarized in Tab. 1. To obtain a fully recrystallized microstructure, the sheet was annealed at 430 °C for 30 min. Prior to mechanical property testing, the texture orientation of the annealed sheet was measured first using a Rigaku D/max 2500PC X-ray diffractometer in the RD-TD plane. The initial mechanical properties of the annealed sheet were measured by the typical tensile and compressive tests along RD, TD and 45° from RD. The dimensions of the specimens used were dog-bone shaped with a gauge length of 8 mm, a gauge width of 5 mm and a gauge thickness of 1.5 mm for the tensile tests (following Chinese National Standard GB/T228.1-2010: Metallic materials: tensile testing at room temperature [41]) and rectangle with a gauge length of 5 mm, a gauge width of 5 mm and a gauge thickness of 1.5 mm for the compressive tests. All the specimens were cut from the surface of the annealed sheet, as shown in Fig. 1a. The applied strain rate was 10^{-3} s^{-1} . An extensometer was used to measure the deformation of the specimens during the tensile tests.

The *in situ* uniaxial and biaxial compression tests were conducted using a self-developed device, as shown in Fig. 1b. The flange ring has two pairs of chutes symmetrically distributed on the inner surface (each pair had two chutes face to face). Two pairs of blocks with bevels are set into the chutes. Each pair of blocks are in the same direction. The bevels match the chutes well

since they have the same inclinations. By rotating the load screw to a specific angle, the flange ring will be pushed forward to a certain distance by the screw. This distance will be transformed to the displacement of the two pairs of blocks toward the center through the matched chutes and bevels. Since all the inclinations are the same, the sample in the center will then deform under BC. Since the load screw is self-locking, the blocks can continue to apply a load on the sample during the whole test. If a pair of blocks is removed, the remaining pair of blocks can offer the sample a uniaxial compressive stress state. The entire device is small enough to be fixed into the sample chamber of the scanning electron microscope (SEM). The strain under UC is calculated along RD and the strain under BC is calculated as the sum of the strains along RD and TD. Thus, it is convenient to do *in situ* morphological observations and EBSD measurements during uniaxial or biaxial compressive tests.

The samples (with RD-5 mm × TD-5 mm × normal direction (ND)-1.5 mm dimension) used for the *in situ* uniaxial compression tests (UC samples) or biaxial compression tests (BC samples) were also cut from the surface of the annealed sheet and mechanically ground in the RD-TD plane. For electro-polishing, a commercial electrolyte ACII from Struers at -20 °C, with a voltage of 20 V for 120 s was applied. The *in situ* uniaxial and biaxial compression were conducted respectively with the same strain rate of 10^{-3} s^{-1} at room temperature. The uniaxial compression tests were along RD. After setting the sample into the device, the initial microstructure of the sample was measured once at the center of the sample using SEM and EBSD. The step size was 0.3 μm . Then, took out the entire device from the chamber. The load screw was then rotated to a certain angle in order to apply a corresponding strain. Then the device was set back into the chamber at the same position for the subsequent measurement. The rotation speed was kept the same to make sure the strain rate of the sample was always 10^{-3} s^{-1} . Since the total strain rate of the sample under BC was the sum of the strain rates along RD and TD, the corresponding rotation speed was half of that under UC. During both of the compression tests, the interrupted equivalent strain was 0, 0.11, 0.16 and 0.21.

3. Results

3.1 Initial mechanical properties and microstructure evolution

Fig. 2 reveals a strong basal texture with a-axis distributing evenly in the RD-TD plane, which infers isotropic mechanical properties in the RD-TD plane. Fig. 3 shows the representative

tensile and compressive true stress-true strain curves of the annealed samples. The yield strength, the ultimate strength and the ultimate strain of the samples along different load directions are comparable. The tensile yield strength is about two times higher than the compressive yield strength. Hence, the sheet is isotropic but asymmetric in the RD-TD plane.

The evolution of the microstructures in the samples during the *in situ* uniaxial and biaxial compression are shown in Fig. 4. It indicates that twinning happens in both samples with increasing strain. The twin percentages under UC and BC are visually comparable. The twin chains in the UC sample tend to be perpendicular to load direction, as shown in Fig. 4b. However, in the BC sample, the directions of the twin chains in the BC sample tend to be random, as shown in Fig. 4f. The identifications of the twin types responding to Fig. 4 are shown in Fig. 5. The extension twin boundaries (ETB), the low or high angle grain boundaries (LAGB or HAGB) with misorientation angle lower or higher than 15° are also presented. It suggests that all the twin variants activated during the compression tests are extension twins (ET). Fig. 6 shows the corresponding evolution of {0002} pole figures (PFs) under UC and BC. It indicates that the initial strong basal texture tilts to RD under UC with increasing ET percentage. With 0.21 strain, there are still some basal texture components, as shown in Fig. 6d. Since the representative orientation of the initial texture is about 10° away from RD, the c-axis poles in the final texture of the deformed UC sample occur a little more than 30° away from RD [42]. However, the poles of the c-axis in the deformed BC sample distribute more evenly in the RD-TD plane, as shown in Fig. 6h. The basal texture components were significantly weakened with increasing biaxial strain. In addition, Fig. 6 also indicates that the texture intensity under BC was weakened faster than that under UC with increasing strain. This indicates that the ET behavior under BC is different from that under UC.

3.2 Extension twinning variant statistical results

Schmid factor (SF) is an important value in the determination of the different behaviors of ET as well as the texture evolution under UC and BC. Since the stress states involved in this paper are complicated, the global SF (GSF) is calculated to investigate the activation of the ET variants as well as basal, prismatic and pyramidal <a+c> slips under UC and BC. The calculation of GSF is:

$$GSF = (b^T \cdot \sigma \cdot n) / \bar{\sigma} \quad (1)$$

$$\bar{\sigma} = \sqrt{\frac{(\sigma_1 - \sigma_2)^2 + (\sigma_2 - \sigma_3)^2 + (\sigma_3 - \sigma_1)^2}{2}} \quad (2)$$

where n is the united ND of the twinning plane and b is the united shearing direction [43]. $\bar{\sigma}$ is the stress intensity used to normalize the stress tensor and σ is the stress tensor of the load applied on the material. For UC along RD and BC in the RD-TD plane in the principal stress space, the corresponding σ are:

$$\sigma_{UC} = \begin{pmatrix} -1 & 0 & 0 \\ 0 & 0 & 0 \\ 0 & 0 & 0 \end{pmatrix} \quad (3)$$

$$\sigma_{BC} = \begin{pmatrix} -1 & 0 & 0 \\ 0 & -1 & 0 \\ 0 & 0 & 0 \end{pmatrix} \quad (4)$$

Since the slip system is bi-directional, the final GSF value in Eq. 1 is an absolute value for slip.

Fig. 7 presents the comparison of the mean GSFs for four deformation modes in the initial and deformed samples under UC and BC. It indicates that under different stress states, the evolution of the mean GSFs are quite different. For instance, with increasing strain, the mean GSF for basal slip slightly increases in the deformed UC sample and decreases in the deformed BC sample. Additionally, the mean GSF for prismatic slip is high in the initial UC sample and low in the initial BC sample. However, after deformation with 0.21 strain, the GSF for prismatic slip decreases to 0.15 under UC but increases rapidly to 0.42 under BC. The GSFs for ET are high in both of the initial samples and decrease with increasing strain. However, the mean GSF for ET in the deformed UC sample is much lower than that in the deformed BC sample, which infers a much stronger geometric hardening effect caused by ET under UC. The most stable mode is pyramidal $\langle a+c \rangle$ slip, which mean GSF changes little despite the stress state and the increasing strain. Hence, the activations of these four deformation mechanisms and their contributions to the plastic flows under UC and BC should be different.

4. Discussion

4.1 The influence of ET activation on the microstructure evolution and mechanical properties under UC and BC

Fig. 6 has revealed the different tendencies of texture evolutions under different stress states. Fig. 4d and h also demonstrates that most of the grains in the deformed samples with 0.21 strain

are the activated ET variants and only a few grains with c-axis parallel to ND remain. Hence, the distributions of the c-axis poles in Fig. 6d and h are in fact the c-axis poles of the ET variants. That is to say, most of the ET variants have the c-axis tilted towards RD after RD compression while the ET variants activated under BC have a greater possibility to tilt their c-axis towards other directions in the RD-TD plane. Fig. 8 also proves that under BC in the RD-TD plane, the GSFs for the six ET variants are all the highest, irrespective of the orientation of the a-axis in the RD-TD plane.

In addition, it is clear from Fig. 6h, the distribution of the c-axis poles is concentrated more along TD. The most important reason for this should be the initial texture, which slightly spreads towards TD. However, the activation of ET, which does not always obey the Schmid law, can also be a reason for this inhomogeneous distribution of c-axis poles [37, 44-46]. Hence, the ET variants that obey the Schmid law under different stress states were identified. During the identification, a grain will be treated as an *obedient grain* to the Schmid law if it meets at least one of the following conditions:

- i) Contains at least one activated ET variant, which has the highest GSF for ET.
- ii) The difference between the GSF of the activated ET variant and the highest GSF is less than 0.05.
- iii) The highest GSF for ET variants is still lower than *zero* and no ET variants are activated in the grain during the whole deformation.

Furthermore, if an activated ET variant meets condition ii), it will be treated as an obedient ET variant. The results of the identifications are shown in Tab. 2. It suggests that both the ratios of the obedient grains and the obedient variants under UC are higher than that under BC, which infers that the change of stress state may have an influence on the obedience of Mg alloys with the Schmid law. Fig. 9 presents the comparison of the mean GSF for the ranked ET variants under UC and BC. Apparently, the difference between the mean GSFs for the six ET variants with different ranks under UC is much higher than that under BC. Under UC, only the GSF for the 2nd ranked ET variant is close to the 1st ranked variant. The fluctuation of the inner stress has a possibility to activate the 2nd ranked ET variant during the uniaxial compression. The mean GSF for the 3rd ranked variant is 50% less than that for the 1st ranked variant and much harder to be activated by the fluctuate inner stress. As a contrast, the GSFs are approximately the same for all the six ET variants and have high values. Even the difference of the GSF between the 1st and

the 6th ranked ET variants is less than 0.10. Hence, the low-ranked ET variants have a much higher possibility to be activated by the fluctuation of the inner stress. This is the main reason why the obedience of Mg alloys to Schmid law under BC is weaker than that under UC at room temperature.

4.2 VPSC-TDT simulation

To better understand the activation of deformation mechanisms in the samples under different stress states, the simulation was produced based on the VPSC-TDT model, which includes deformation mechanisms of both twinning and de-twinning (TDT). Wang *et al.* [47] reported the full description of the VPSC-TDT mode. Regardless of twinning and slip, the shear strain rate of system α can be described as:

$$\dot{\gamma}^{\alpha} = \dot{\gamma}_0 |\tau^{\alpha} / \tau_{cr}^{\alpha}|^n \text{sgn}(\tau^{\alpha}) \quad (5)$$

where $\dot{\gamma}_0$ is a reference shear rate, τ_{cr}^{α} is CRSS of system α and n is the strain rate sensitivity ($n=20$ in this paper). For both slip and twinning, the evolution of τ_{cr}^{α} is given by:

$$\dot{\tau}_{cr}^{\alpha} = \frac{d\hat{\tau}^{\alpha}}{d\Gamma} \sum_{\beta} h^{\alpha\beta} |\dot{\gamma}^{\beta}| \quad (6)$$

where $\Gamma = \sum_{\alpha} \int |\dot{\gamma}^{\alpha}| dt$ is the accumulated shear strain in the grain and $h^{\alpha\beta}$ are the latent hardening coupling coefficients, which empirically account for the obstacles on system α associated with system β . $\hat{\tau}^{\alpha}$ is the threshold stress and characterized by the Voce hardening law:

$$\hat{\tau}^{\alpha} = \tau_0^{\alpha} + (\tau_1^{\alpha} + \theta_1^{\alpha} \Gamma) (1 - \exp(-\theta_0^{\alpha} \Gamma / \tau_1^{\alpha})) \quad (7)$$

where τ_0^{α} , $\tau_0^{\alpha} + \tau_1^{\alpha}$, θ_0^{α} and θ_1^{α} are the initial CRSS, the back-extrapolated CRSS, the initial hardening rate and the asymptotic hardening rate, respectively. Since it is rare that a grain can be fully twinned, the VPSC-TDT defines a threshold twin volume fraction V^{th} as:

$$V^{th} = \min(1.0, A_1 + A_2 V^{eff} / V^{acc}) \quad (8)$$

where A_1 and A_2 are two material constants [47]. V^{acc} and V^{eff} are the weighted volume fraction of the twinned region and volume fraction of twin-terminated grains, respectively. Tab. 3 presents the parameters used for the VPSC-TDT simulations corresponding to the AZ31 sheet

with strong basal texture. The latent hardening coupling coefficient among slips and twinning are all set to 1 since the self and latent hardening are indistinguishable [47-50].

As shown in Fig. 10a, the VPSC-TDT model can reproduce well the experimental curves of the annealed sheet under UC and UT along RD and TD. Therefore, the increasing flow stresses along RD and TD with increasing total strain under UC and BC are calculated, as presented in Fig. 10b. The ultimate strains corresponding to the flow stress along RD and TD under BC are equal to 0.105, which produce a total strain of 0.21. It is thus apparent that the yielding strength under BC is lower than that under UC. The main reason should be the relatively higher GSFs for basal slip and all the six ET variants under BC. The stages of the stress-strain curves under BC in Fig. 10b should be the result of the different behavior of the ET variants, which lead to the switching of the activated slip systems. The distribution of the experimental and the simulated textures with 0.21 strain under UC and BC are also very close, as shown in Fig. 10c and d. Hence, the VPSC-TDT model is reliable to describe the behavior of the samples under UC and BC.

Fig. 11 presents the calculated relative activities of the deformation mechanisms during uniaxial and biaxial compression. It indicates that basal $\langle a \rangle$ slip and ET offer the most strain accommodation at the beginning of deformation under UC and BC. With the strain being over 0.05, the relative activity of ET decreases rapidly. The relative activity of basal slip keeps increasing under UC while decreases under BC. Furthermore, with increasing strain, pyramidal $\langle a+c \rangle$ slip is activated to offer necessary strain accommodation under UC. However, under BC, it is prismatic $\langle a \rangle$ which joins to coordinate the plastic flow. According to Tab. 3, the CRSS of prismatic $\langle a \rangle$ is lower than pyramidal $\langle a+c \rangle$ slip. Hence, the corresponding flow stresses under BC are lower than that under UC. Fig. 12 shows the total relative activity of each deformation mode to the strain of 0.21 under UC and BC. The total activity of basal slip is 67.1% under UC and 35.6% strain under BC. The total activity of pyramidal $\langle a+c \rangle$ slip is about 9.3% strain under UC and that of prismatic slip under BC is about 35.3%. The activity of ET under UC (22.8%) is lower than that under BC (28.4%). Hence, the main deformation modes and their contribution to the plastic flow are quite different under UC and BC.

4.3 Evolution of GND density from EBSD data under UC and BC

The local orientation in these samples may be different as well for the different main deformation mechanisms under different stress states. It has been reported that microstructure heterogeneity had a link with strain gradient evolution and subsequent generation of GNDs during the plastic deformation [51-55]. In this study, the local misorientation was determined using the kernel average misorientation (KAM) from the EBSD orientation data [56]. The local misorientation of every single point ($300 \times 300 \text{ nm}^2$) was determined by 8 surrounding points:

$$\theta_0 = \frac{\sum_{i=1}^8 \theta_i \cdot I_{(\theta_i < \alpha)}}{\sum_{i=1}^8 I_{(\theta_i < \alpha)}} \quad (9)$$

Where θ_0 is the resulted local misorientation for the corresponding point. θ_i is the misorientation between this point and its neighbor point i . $I_{(\theta_i < \alpha)}$ is an indicator function and is the misorientation threshold (2° here) used to eliminate the interference of grain boundary [55]. The GND density was calculated as [56]:

$$\rho = \frac{2\theta}{\mu b} \quad (10)$$

Where μ is the step size and b is the magnitude of the Burgers vector ($b=0.107 \text{ nm}$ in this paper).

The calculated GND density maps with increasing strain under UC and BC are shown in Fig. 13. It indicates that the GND densities in both of the initial samples are low. With increasing strain, the densities of GND increase rapidly. Comparing with Fig. 13 a-d and e-h, it seems that the density of GND in the UC sample increases faster than that in the BC sample. In addition, the distribution of GNDs are inhomogeneous in both samples. Fig. 14 shows the histogram distribution of GND density for each map. The mean values in Fig. 14a and e reveal that the initial GND densities are close to each other. While the density in the UC sample indeed increases faster than that in the BC sample with increasing strain. This indicates that for coordinating the same macroscopic plastic strain, dislocations are needed to be activated more under UC than under BC. The main reason is that the activation of ET under BC is much easier than that under UC. Fig. 12 has suggested that the strain coordinated by ET under BC is higher than that under UC. Hence, less slip is needed to be activated under BC.

Fig. 14 also indicates that the standard deviation of the GND density in the BC sample is always lower than that in the UC sample with the same strain. With increasing strain, this difference increases as well. This infers that the distribution of GND or the microscopic strain in the UC sample is more inhomogeneous than that in the BC sample with increasing strain. One

important reason is that the activation of ET under BC is more than that under UC. The CRSS of ET is relatively low. The stress concentration caused by the shearing of ET is at a lower level. Besides, the strain compatibility between different ET variants is easier to be activated as well for the high GSF for all the variants under BC. This further releases the stress concentration. The other important reason is that the activation of prismatic slip under BC leads to a lower flow stress than that under UC during the later deformation, which can reduce the GND density as well.

4.4 Interactions among the deformation mechanisms under UC and BC

It has been proved that the activation of ET under BC led to different reorientation of the texture to that under UC. The relationship between the different change of GSFs and the activation of the deformation modes needs to be examined. However, both the CRSSes of the deformation mechanisms and the flow stresses change during the deformation for the strain hardening effect. Hence, Tab. 4 presents the detailed CRSSes of the deformation mechanisms calculated using Eq. 7 under UC and BC. The increasing flow stresses along RD and TD with increasing strain are listed in Tab. 5. It should be noted that the strain values in Tab. 4 and Tab. 5 are the sum of the elastic strain and the plastic strain. The ultimate elastic strain (0.04) of the UC sample is easy to get from Fig. 10a. However, the ultimate elastic strain of the BC sample is unclear since the device is without stress sensors and VPSC-TDT model does not involve the elastic strain, either. It has been reported that the elastic modulus under biaxial stress state was much higher than that under uniaxial stress state [36, 57]. Fig. 10b also indicates that the yielding strength under BC is lower than that under UC. Hence, the ultimate elastic strain under BC should be lower than that under UC and is set as 0.02 (0.01 along RD and 0.01 along TD) in this paper.

Based on the above data, Fig. 15 presents the distribution of the grains, in which the corresponding deformation mechanisms are possible to be activated under UC or BC with increasing macroscopic strain. It indicates that basal slip is possible to be activated in most grains during the whole uniaxial compression while is activated less and less during the biaxial compression. This difference should be attributed to the different stress state. When a material is applied a complicated load, the total effect of the loads on a shearing plane in the material can be described using the concept “total stress”, which is calculated using Eq. 11 [58]:

$$S = \sigma \cdot n \quad (11)$$

where n is the normal direction of the twinning or slip plane. The component of the total stress along the slip or the twinning direction is the resolved shear stress of the load on the corresponding mechanism.

Under uniaxial stress state, the total stress in any plane is parallel to the uniaxial load [37]. For the initial strong basal texture, the angle between the basal plane and the total stress is close to 0° and the initial mean GSF for basal slip is low. After the UC compression, the angle between the basal plane and the total stress is generally in the range of $60^\circ \sim 90^\circ$ in most ET variants, as shown in Fig. 16a. Hence, the mean GSF for basal slip increases with increasing strain. However, the total stress in the basal plane is always parallel to the component of the corresponding n in the RD-TD plane under BC. Since most of the basal planes are nearly perpendicular to the RD-TD plane in the deformed BC sample, the total stress in the basal plane is also perpendicular to the basal plane under BC, as shown in Fig. 16b. Hence, the mean GSF for basal slip under BC decreases gradually with increasing strain.

In addition, the possibilities of ET to be activated are high in both initial samples and decrease with increasing strain in a similar way. However, the activation of prismatic slip in both samples changes oppositely. In the initial UC sample, the GSF for prismatic slip is high for the grains with c-axis parallel to ND as shown in Fig. 15a. While under BC, prismatic slip can only be activated in the activated ET variants, as shown in Fig. 15d. With increasing strain, the ET percentages increase in both samples. The possibility of prismatic slip to be activated decreases in the UC sample while increase in the BC sample. This indicates that the appearance of the ET variants limits the activation of prismatic slip under UC while facilitates the activation of prismatic slip under BC. This difference should also be attributed to the stress state and the strong basal texture.

As shown in Fig. 17, under UC along RD, the distributions of high GSFs for prismatic slip and ET are both along TD. The c-axis poles of the activated ET variants are in the regions with low GSF for prismatic slip. However, under BC, the distribution of high GSF for prismatic slip is around the edge of the PF while for ET is at the center. After the biaxial compression, all the c-axis of the activated ET variants tilt into the regions with high GSF for prismatic slip. Hence, the activation of prismatic slip in the ET variants under BC is much easier than that under UC. Additionally, since ET and prismatic slip are not able to be activated at high strain level in the

deformed UC sample, pyramidal slip is activated to coordinate the plastic flow. This is also why the flow stress under BC is lower than that under UC at the later stage of deformation. With the better deformation compatibility, the lower flow stress, yield strength and GND density, the AZ31 rolled sheet shows better deformability under BC than that under UC.

5. Conclusion

The evolution of the microstructures in AZ31 rolled sheet with strong basal texture was obtained using *in situ* EBSD measurements under UC and BC. The activation of the deformation mechanisms as well as the strain hardening effect were calculated using a VPSC-TDT model. Based on the results, the activation of ET variants, the GND density and the interactions between different deformation modes were systemically examined. The conclusions were as follows:

- 1) At room temperature, the evolution of the strong basal texture in the AZ31 rolled sheet under BC was different from that under UC. After the biaxial compression, the orientation of the c-axis of most grains was distributed randomly in the RD-TD plane. As a compression, most of the c-axis tilted towards RD after the uniaxial compression along RD. The main reason for this was the different behavior of ET variants under different stress states.
- 2) The mean GSF for basal slip increased during the uniaxial compression while it decreased during the biaxial compression. As a contrast, the mean GSF for prismatic slip decreased under UC while it increased under BC with increasing strain. The mean GSF for ET decreased under both stress states. However, the final GSF for ET under UC was much lower than that under BC. In addition, the obedience of ET to the Schmid law under BC was proved weaker than that under UC. These differences were the results of the combination of the stress state and the strong basal texture.
- 3) The activated ETs offered more deformation compatibility under BC. This further led to lower GND density, more homogeneous distribution of the microscopic strain and lower flow stress. Especially, the equivalent yield strength of the sheet with strong basal texture under BC was also lower than that under UC since the GSFs were approximately the same and high for all the six ET variants under BC.
- 4) The interactions between the deformation mechanisms were dominated by the stress state. During the deformation, the reorientation caused by the activation of ET limited the

activation of prismatic slip under UC while facilitated prismatic slip under BC. This was why pyramidal $\langle a+c \rangle$ slip was activated at the later stage of deformation under UC and the flow stress was higher than that under BC as well. The lower GND density, more homogeneous strain distribution, better deformation compatibility, lower yield strength and lower flow stress inferred a better deformability of the AZ31 rolled sheet under BC at room temperature. Hence, the application of biaxial compressive stress state could be considered to improve the deformability and limit the flow stress during the processing (i.e. drawing, forging) of Mg alloys at room temperature.

Acknowledgements

This work was supported by The National Key Research and Development Plan (2016YFB0301104) and the National Natural Science Foundation of China (No. 51671041 , No. 51531002 and No. U1764253). The China Scholarship Council is also gratefully acknowledged for financial support for Dabiao Xia (201806050045).

Reference

- [1] H. Dieringa, N. Hort, D. Letzig, J. Bohlen, D. Höche, C. Blawert, M. Zheludkevich, K.U. Kainer, Mg Alloys: Challenges and Achievements in Controlling Performance, and Future Application Perspectives, TMS Annual Meeting & Exhibition, Springer, 2018, pp. 3-14.
- [2] K. Singh, G. Singh, H. Singh, Review on friction stir welding of magnesium alloys, *J Magnes Alloy* 6(4) (2018) 399-416.
- [3] A. Imandoust, C.D. Barrett, T. Al-Samman, K.A. Inal, H. El Kadiri, A review on the effect of rare-earth elements on texture evolution during processing of magnesium alloys, *J Mater Sci* 52(1) (2017) 1-29.
- [4] S.H. You, Y.D. Huang, K.U. Kainer, N. Hort, Recent research and developments on wrought magnesium alloys, *J Magnes Alloy* 5(3) (2017) 239-253.
- [5] G. Zhang, Y. Wang, Z. Liu, S. Liu, Influence of Al addition on solidification path and hot tearing susceptibility of Mg-2Zn-(3+ 0.5 x) Y-xAl alloys, *J Magnes Alloy* (2019).
- [6] W. Ren, J. Li, R. Xin, Texture dependent shifting behavior of neutral layer in bending of magnesium alloys, *Scripta Mater* 170 (2019) 6-10.
- [7] L.L.C. Catorceno, H.F.G. de Abreu, A.F. Padilha, Effects of cold and warm cross-rolling on microstructure and texture evolution of AZ31B magnesium alloy sheet, *J Magnes Alloy* 6(2) (2018) 121-133.
- [8] Z.M. Wang, R.Y. Gu, S.C. Chen, W.R. Wang, X.C. Wei, Effect of upper-die temperature on the formability of AZ31B magnesium alloy sheet in stamping, *J Mater Process Tech* 257 (2018) 180-190.
- [9] E. Ball, P. Prangnell, Tensile-compressive yield asymmetries in high strength wrought magnesium alloys, *Scripta Metallurgica et Materialia;(United States)* 31(2) (1994).
- [10] X.Y. Lou, M. Li, R.K. Boger, S.R. Agnew, R.H. Wagoner, Hardening evolution of AZ31B Mg sheet, *Int J Plasticity* 23(1) (2007) 44-86.

- [11] C.M. Cepeda-Jimenez, C. Prado-Martinez, M.T. Perez-Prado, Understanding the high temperature reversed yield asymmetry in a Mg-rare earth alloy by slip trace analysis, *Acta Mater* 145 (2018) 264-277.
- [12] L.F. Wang, E. Mostaed, X.Q. Cao, G.S. Huang, A. Fabrizi, F. Bonollo, C.Z. Chi, M. Vedani, Effects of texture and grain size on mechanical properties of AZ80 magnesium alloys at lower temperatures, *Mater Design* 89 (2016) 1-8.
- [13] A. Javaid, F. Czerwinski, Effect of hot rolling on microstructure and properties of the ZEK100 alloy, *J Magnes Alloy* 7(1) (2019) 27-37.
- [14] W.F. Hosford, *The mechanics of crystals and textured polycrystals*, Oxford University Press(USA), 1993 (1993) 248.
- [15] C.N. Tome, P.J. Maudlin, R.A. Lebensohn, G.C. Kaschner, Mechanical response of zirconium - I. Derivation of a polycrystal constitutive law and finite element analysis, *Acta Mater* 49(15) (2001) 3085-3096.
- [16] J. Bohlen, M.R. Nurnberg, J.W. Senn, D. Letzig, S.R. Agnew, The texture and anisotropy of magnesium-zinc-rare earth alloy sheets, *Acta Mater* 55(6) (2007) 2101-2112.
- [17] V.M. Miller, T.D. Berman, I.J. Beyerlein, J.W. Jones, T.M. Pollock, Prediction of the plastic anisotropy of magnesium alloys with synthetic textures and implications for the effect of texture on formability, *Mat Sci Eng a-Struct* 675 (2016) 345-360.
- [18] O. Cazacu, J.A. Rodriguez-Martinez, Effects of plastic anisotropy on localization in orthotropic materials: New explicit expressions for the orientation of localization bands in flat specimens subjected to uniaxial tension, *J Mech Phys Solids* 126 (2019) 272-284.
- [19] S. Kurukuri, M.J. Worswick, D.G. Tari, R.K. Mishra, J.T. Carter, Rate sensitivity and tension-compression asymmetry in AZ31B magnesium alloy sheet, *Philos T R Soc A* 372(2015) (2014).
- [20] X. Wang, L. Jiang, D.L. Zhang, I.J. Beyerlein, S. Mahajan, T.J. Rupert, E.J. Lavernia, J.M. Schoenung, Reversed compressive yield anisotropy in magnesium with microlaminated structure, *Acta Mater* 146 (2018) 12-24.
- [21] S. Graff, W. Brocks, D. Steglich, Yielding of magnesium: From single crystal to polycrystalline aggregates, *Int J Plasticity* 23(12) (2007) 1957-1978.
- [22] W.J.M. Tegart, Independent Slip Systems + Ductility of Hexagonal Polycrystals, *Philos Mag* 9(98) (1964) 339-&.
- [23] S.K. Sahoo, L.S. Toth, S. Biswas, An analytical model to predict strain-hardening behaviour and twin volume fraction in a profoundly twinning magnesium alloy, *Int J Plasticity* (2019).
- [24] K. Sofinowski, T. Panzner, M. Kubenova, J. Capek, S. Van Petegem, H. Van Swygenhoven, In situ tension-tension strain path changes of cold-rolled Mg AZ31B, *Acta Mater* 164 (2019) 135-152.
- [25] O.E.a.V. Randle, *Introduction to texture analysis : macrotexture, microtexture, and orientation mapping*, Taylor & Francis Group 2 (2010) 34-36.
- [26] M.A. Kumar, I.J. Beyerlein, C.N. Tome, A measure of plastic anisotropy for hexagonal close packed metals: Application to alloying effects on the formability of Mg, *J Alloy Compd* 695 (2017) 1488-1497.
- [27] Q. Yu, L. Qi, R.K. Mishra, J. Li, A.M. Minor, Reducing deformation anisotropy to achieve ultrahigh strength and ductility in Mg at the nanoscale, *P Natl Acad Sci USA* 110(33) (2013) 13289-13293.
- [28] I.J. Beyerlein, R.J. McCabe, C.N. Tome, Effect of microstructure on the nucleation of deformation twins in polycrystalline high-purity magnesium: A multi-scale modeling study, *J Mech Phys Solids* 59(5) (2011) 988-1003.
- [29] Q. Sun, A. Ostapovets, X.Y. Zhang, L. Tan, Q. Liu, Investigation of twin-twin interaction in deformed magnesium alloy, *Philos Mag* 98(9) (2018) 741-751.
- [30] M.Y. Gong, G.S. Liu, J. Wang, L. Capolungo, C.N. Tome, Atomistic simulations of interaction between basal <a> dislocations and three-dimensional twins in magnesium, *Acta Mater* 155 (2018) 187-198.

- [31] G. Nayyeri, W.J. Poole, C.W. Sinclair, S. Zaefferer, Measurement of the critical resolved shear stress for basal slip in magnesium alloys using instrumented indentation, *Scripta Mater* 156 (2018) 37-41.
- [32] B. Tang, Y. He, W.A. Goddard III, Q. An, First principles predicting enhanced ductility of boride carbide through magnesium microalloying, *Journal of the American Ceramic Society* (2019).
- [33] M. Merklein, M. Biasutti, Development of a biaxial tensile machine for characterization of sheet metals, *J Mater Process Tech* 213(6) (2013) 939-946.
- [34] M. Cakmak, M. Hassan, E. Unsal, C. Martins, A fast real time measurement system to track in and out of plane optical retardation/birefringence, true stress, and true strain during biaxial stretching of polymer films (vol 83, 123901, 2012), *Rev Sci Instrum* 87(11) (2016).
- [35] A. Smits, D. Van Hemelrijck, T.P. Philippidis, A. Cardon, Design of a cruciform specimen for biaxial testing of fibre reinforced composite laminates, *Compos Sci Technol* 66(7-8) (2006) 964-975.
- [36] D. Steglich, Y. Jeong, M.O. Andar, T. Kuwabara, Biaxial deformation behaviour of AZ31 magnesium alloy: Crystal-plasticity-based prediction and experimental validation, *Int J Solids Struct* 49(25) (2012) 3551-3561.
- [37] D.B. Xia, G.S. Huang, Q.Y. Deng, B. Jiang, S.S. Liu, F.S. Pan, Influence of stress state on microstructure evolution of AZ31 Mg alloy rolled sheet during deformation at room temperature, *Mat Sci Eng a-Struct* 715 (2018) 379-388.
- [38] D. Xia, G. Huang, S. Liu, A. Tang, S. Gavras, Y. Huang, N. Hort, B. Jiang, F. Pan, Microscopic deformation compatibility during biaxial tension in AZ31 Mg alloy rolled sheet at room temperature, *Materials Science and Engineering: A* (2019).
- [39] Y.Q. Jia, Y.L. Bai, Experimental study on the mechanical properties of AZ31B-H24 magnesium alloy sheets under various loading conditions, *Int J Fracture* 197(1) (2016) 25-48.
- [40] Z.-Z. Shi, J.-Y. Xu, J. Yu, X.-F. Liu, Intragranular cross-level twin pairs in AZ31 Mg alloy after sequential biaxial compressions, *J Alloy Compd* 749 (2018) 52-59.
- [41] GB/T 228.1-2010, 2010, Metallic materials—Tensile testing—Part 1: Method of test at room temperature, Beijing, China, Standardization Administration. [in Chinese].
- [42] S.G. Hong, S.H. Park, C.S. Lee, Role of {10-12} twinning characteristics in the deformation behavior of a polycrystalline magnesium alloy, *Acta Mater* 58(18) (2010) 5873-5885.
- [43] D. Xia, X. Chen, G. Huang, B. Jiang, A. Tang, H. Yang, S. Gavras, Y. Huang, N. Hort, F. Pan, Calculation of Schmid factor in Mg alloys: Influence of stress state, *Scripta Mater* 171 (2019) 31-35.
- [44] C.D. Barrett, H. El Kadiri, M.A. Tschopp, Breakdown of the Schmid law in homogeneous and heterogeneous nucleation events of slip and twinning in magnesium, *J Mech Phys Solids* 60(12) (2012) 2084-2099.
- [45] C. Lou, X.Y. Zhang, Y. Ren, Non-Schmid-based {10-12} twinning behavior in polycrystalline magnesium alloy, *Mater Charact* 107 (2015) 249-254.
- [46] K.D. Molodov, T. Al-Samman, D.A. Molodov, G. Gottstein, On the role of anomalous twinning in the plasticity of magnesium, *Acta Mater* 103 (2016) 711-723.
- [47] H. Wang, P.D. Wu, J. Wang, C.N. Tome, A crystal plasticity model for hexagonal close packed (HCP) crystals including twinning and de-twinning mechanisms, *Int J Plasticity* 49 (2013) 36-52.
- [48] N. Bertin, C.N. Tome, I.J. Beyerlein, M.R. Barnett, L. Capolungo, On the strength of dislocation interactions and their effect on latent hardening in pure Magnesium, *Int J Plasticity* 62 (2014) 72-92.
- [49] A. Chapuis, Z.Q. Wang, Q. Liu, Influence of material parameters on modeling plastic deformation of Mg alloys, *Mat Sci Eng a-Struct* 655 (2016) 244-250.
- [50] Y. Lian, L. Hu, T. Zhou, M.B. Yang, J. Zhang, Numerical Investigation of Secondary Deformation Mechanisms on Plastic Deformation of AZ31 Magnesium Alloy Using Viscoplastic Self-Consistent Model, *Metals-Basel* 9(1) (2019).
- [51] M.F. Ashby, The deformation of plastically non-homogeneous materials, *The Philosophical Magazine: A Journal of Theoretical Experimental and Applied Physics* 21(170) (1970) 399-424.

- [52] N.A. Fleck, G.M. Muller, M.F. Ashby, J.W. Hutchinson, Strain gradient plasticity: Theory and experiment, *Acta Metall Mater* 42(2) (1994) 475-487.
- [53] W.D. Nix, H. Gao, Indentation size effects in crystalline materials: A law for strain gradient plasticity, *J Mech Phys Solids* 46(3) (1998) 411-425.
- [54] H. Gao, Y. Huang, W.D. Nix, J.W. Hutchinson, Mechanism-based strain gradient plasticity— I. Theory, *J Mech Phys Solids* 47(6) (1999) 1239-1263.
- [55] X. Ma, C. Huang, J. Moering, M. Ruppert, H.W. Höppel, M. Göken, J. Narayan, Y. Zhu, Mechanical properties of copper/bronze laminates: Role of interfaces, *Acta Mater* 116 (2016) 43-52.
- [56] M. Calcagnotto, D. Ponge, E. Demir, D. Raabe, Orientation gradients and geometrically necessary dislocations in ultrafine grained dual-phase steels studied by 2D and 3D EBSD, *Materials Science and Engineering: A* 527(10) (2010) 2738-2746.
- [57] J.Y. Min, T.B. Stoughton, J.E. Carsley, B.E. Carlson, J.P. Lin, X.L. Gao, Accurate characterization of biaxial stress-strain response of sheet metal from bulge testing, *Int J Plasticity* 94 (2017) 192-213.
- [58] G.E. Dieter, *Mechanical Metallurgy Si Metric Edition*, McGraw-Hill Book Company (1988) 28-29.

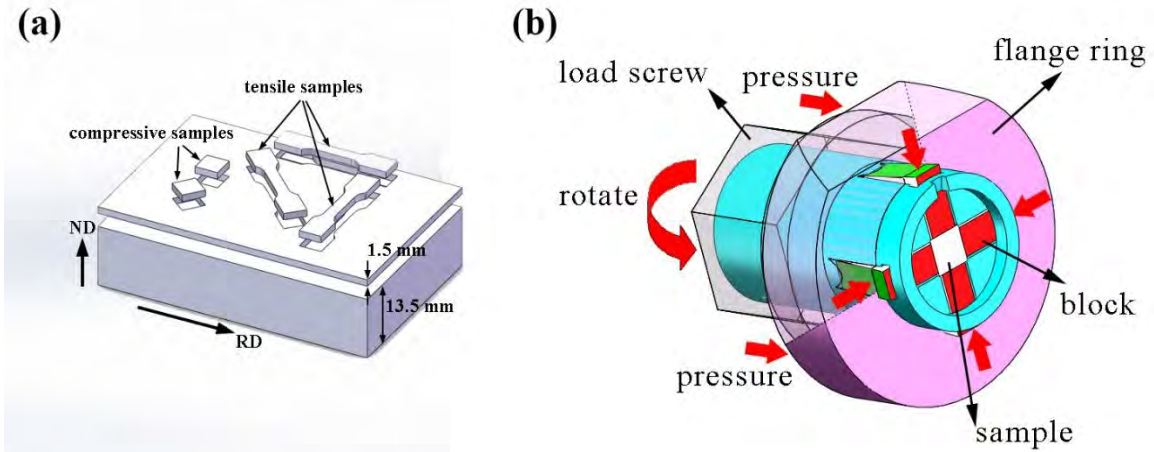


Fig. 1. Schematic diagrams of (a) samples cut from the annealed sheet and (b) the *in situ* compression device using compressive samples.

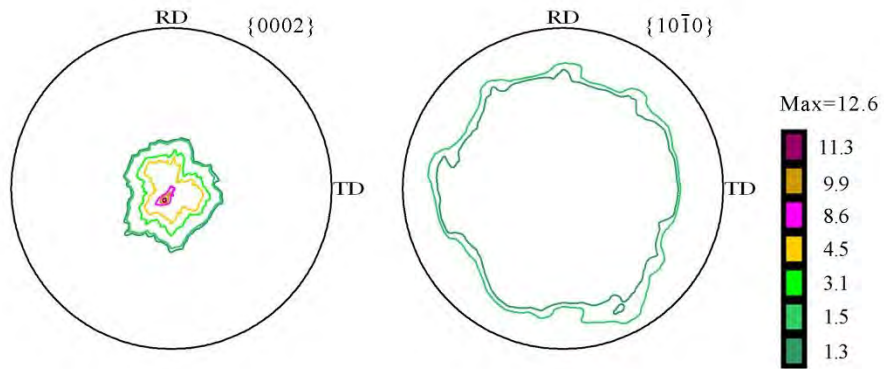


Fig. 2. The {0002} and {10-10} pole figures of the annealed AZ31 rolled sheet measured by the X-ray diffractometer.

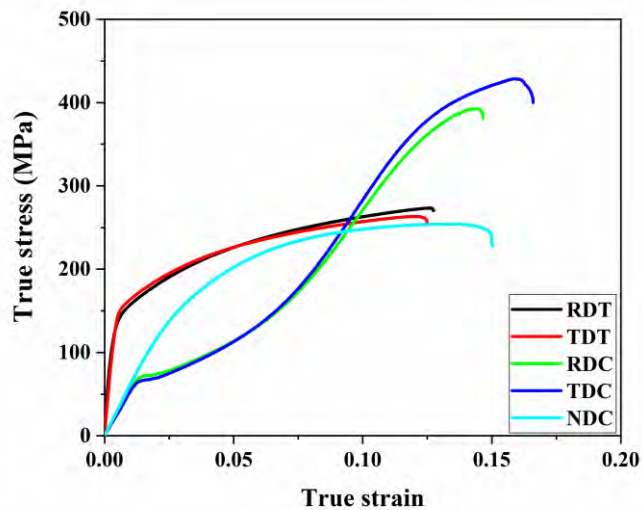


Fig. 3. Typical compressive and tensile true stress-true strain curves of annealed AZ31 rolled sheet with 1.5 mm gauge thickness.

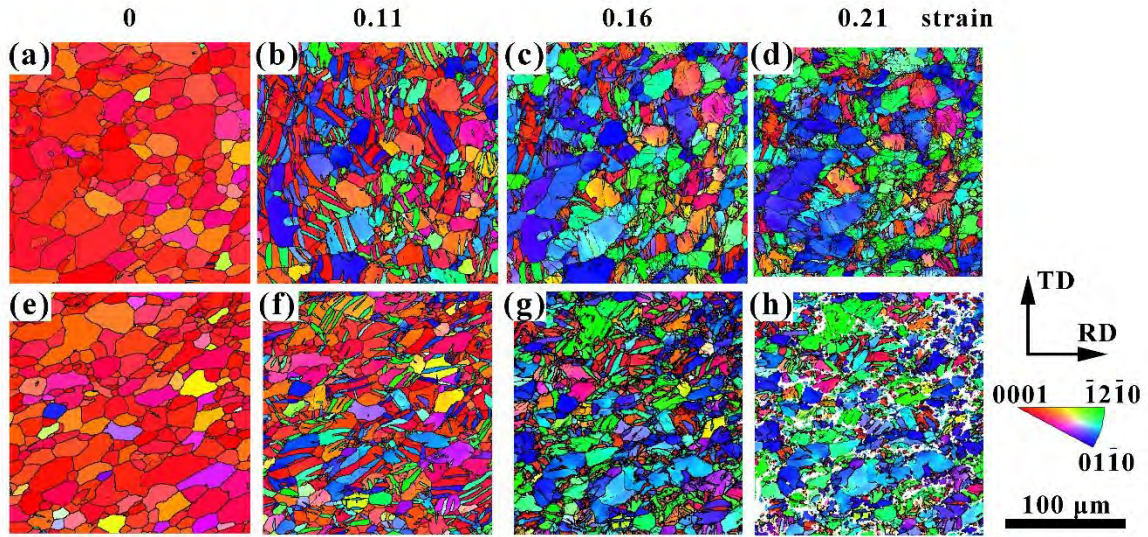


Fig. 4. The *in situ* inverse pole figures of the samples with different strain level under UC and BC with increasing strain. The load is along RD under UC.

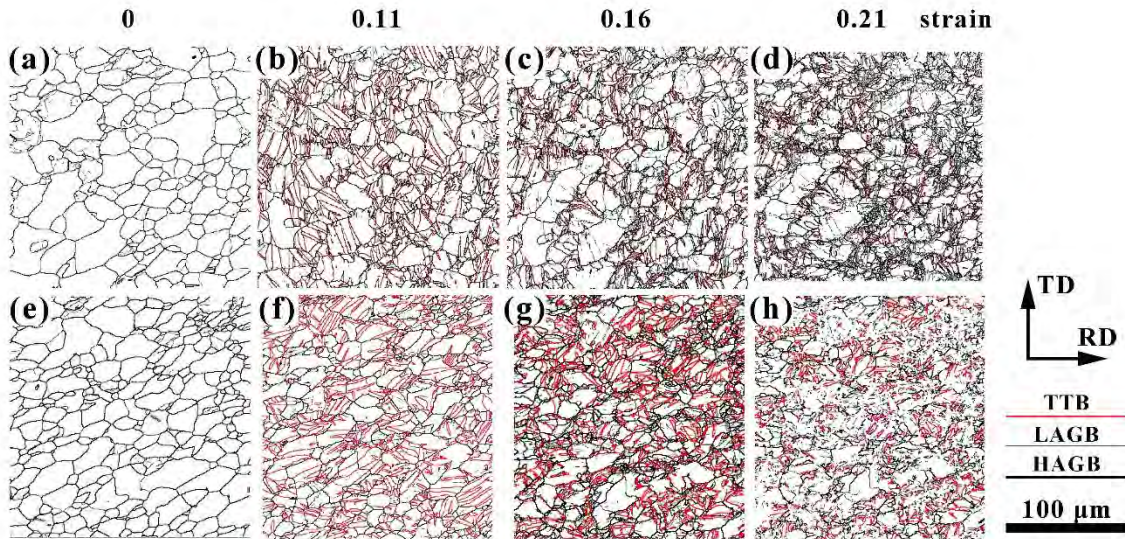


Fig. 5. ETB, LAGB and HAGB evolutions of samples under UC (a-d) and BC (e-h) with increasing strain.

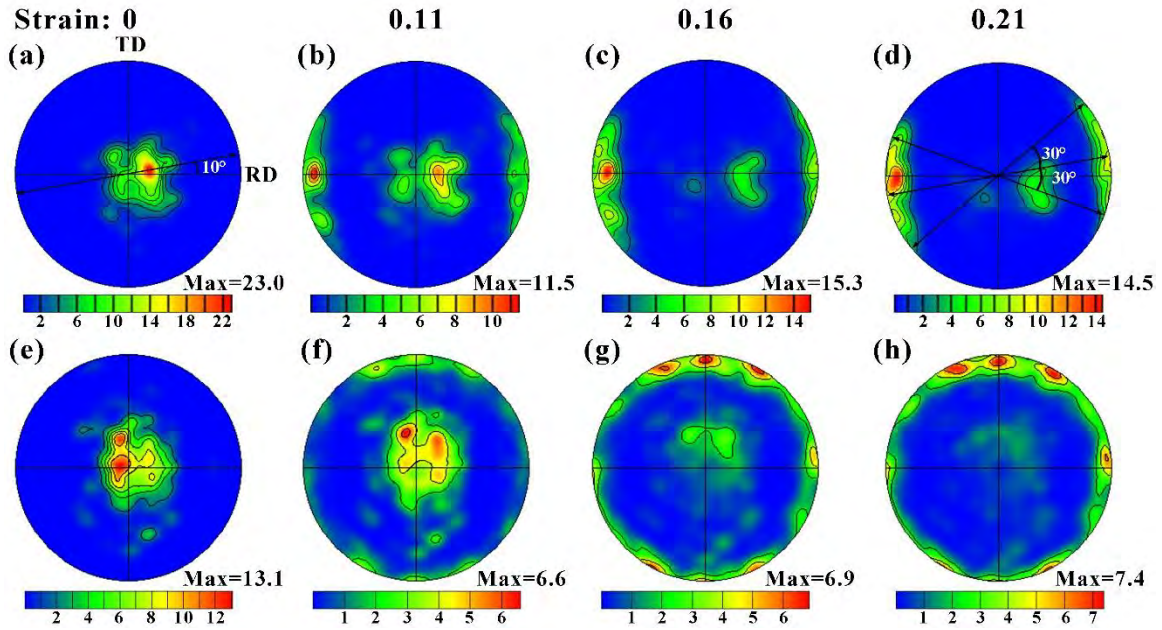


Fig. 6. The evolution of the $\{0002\}$ PFs in the AZ31 rolled sheets with increasing strain under UC (a-d) and BC (e-h).

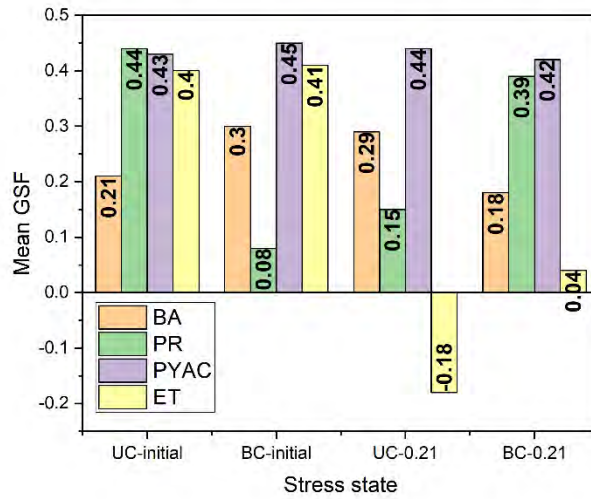


Fig. 7. The mean GSFs for basal (BA), prismatic (PR), pyramidal $\langle a+c \rangle$ (PYAC) slips and ET in the initial and the deformed (0.21 strain) samples.

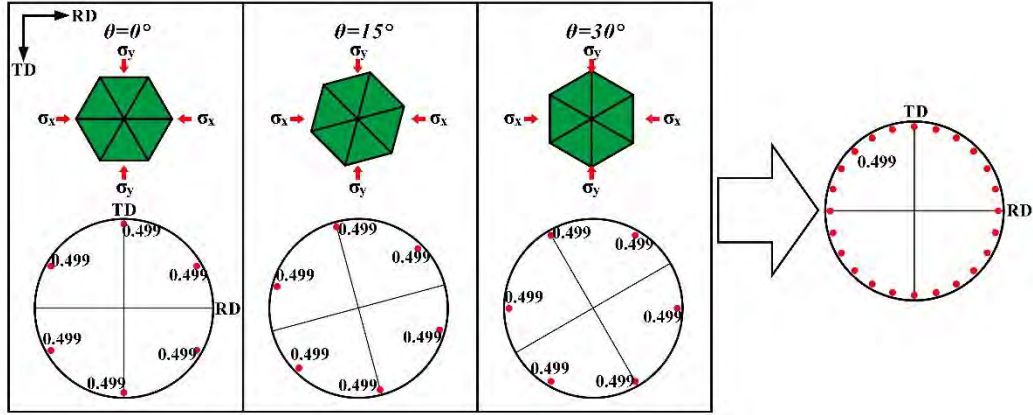


Fig. 8. GSF analysis on the six ET variants with different θ angles between a-axis and RD in the initial strong basal texture under BC. When the c-axis is parallel to ND, the change of θ will have no obvious influence on the high GSF values for the six ET variants, as shown in the left three PFs. Hence, the activation of the six ET variants **all have** high possibilities in the AZ31 sheet under BC, as shown in the rightmost PF.

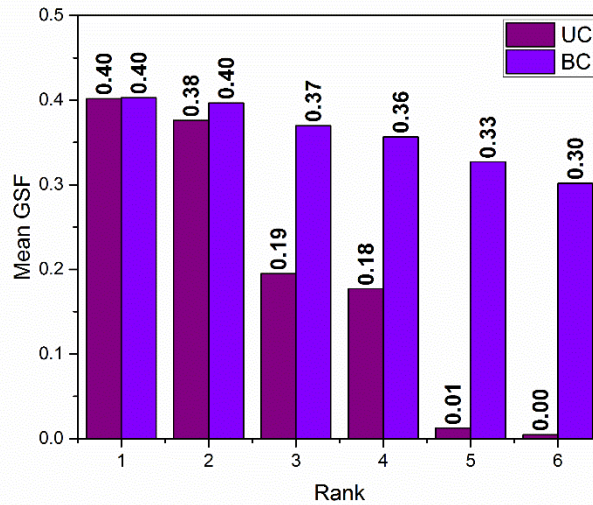


Fig. 9. The comparison of the mean GSF for the ranked ET variants under UC and BC.

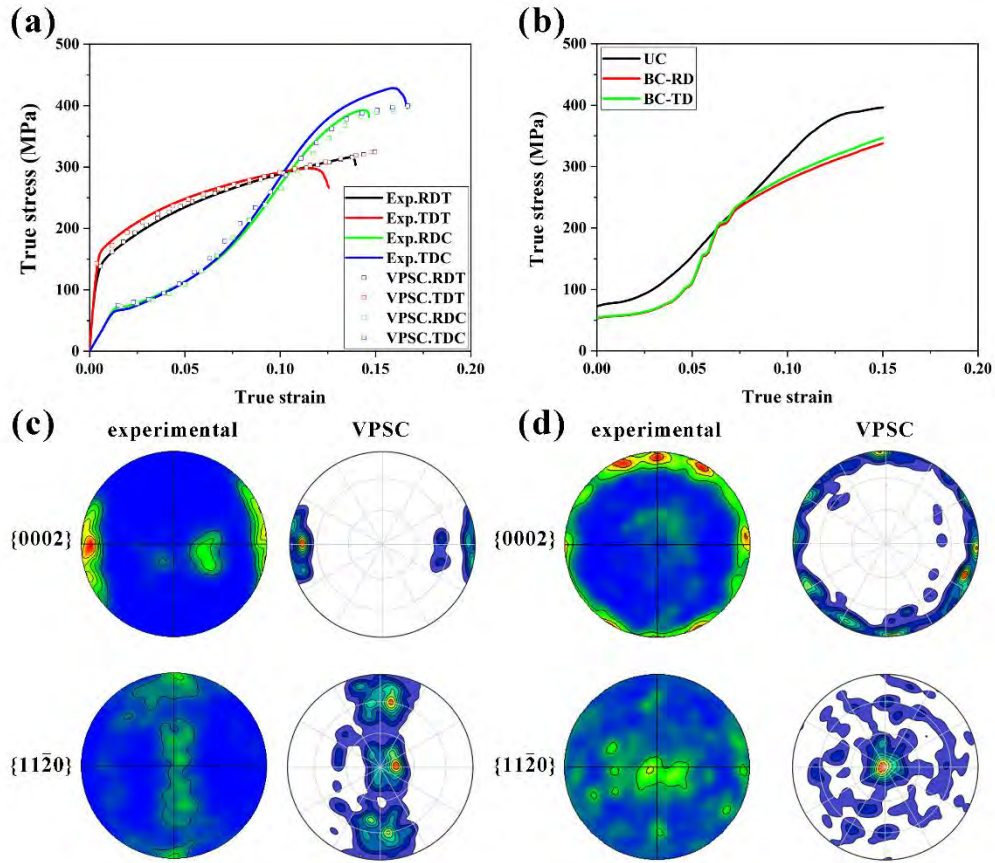


Fig. 10. The comparison between (a) the measured and fitted true stress-true strain curves under UC and UT along RD and TD; (b) the simulated true stress-true strain curves along RD and TD under different UC and BC; (c) the measured and the simulated texture of the deformed sample with 0.21 strain under UC and (d) the measured and the simulated texture of the deformed sample with 0.21 strain under BC.

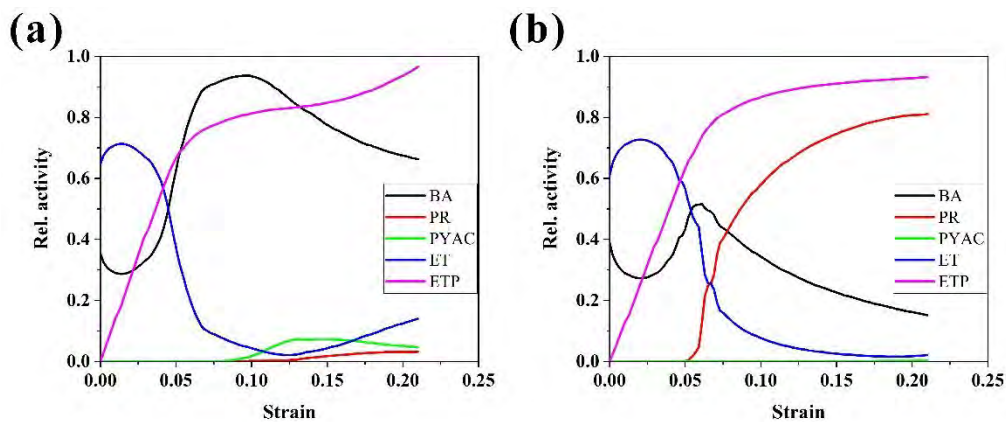


Fig. 11. Relative activities under (a) UC and (b) BC based on the VPSC-TDT simulation.

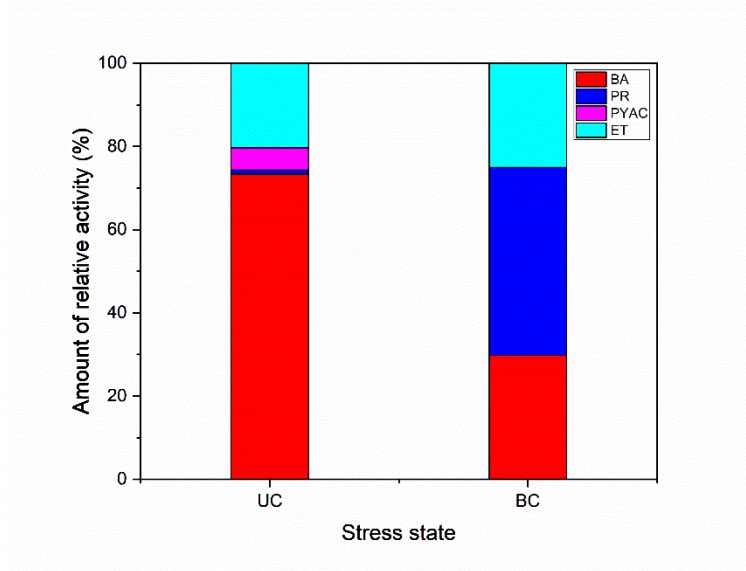


Fig. 12. Relative activity of each deformation mode to strain of 0.21 under UC and BC.

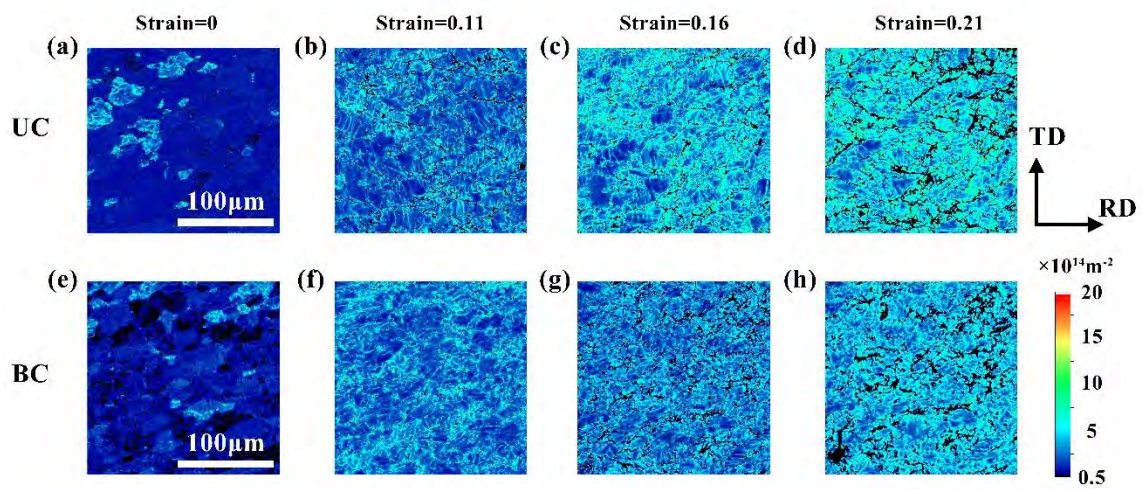


Fig. 13. GND density mapping based on local misorientation results in (a-d) UC sample and (e-h) BC sample with increasing strain.

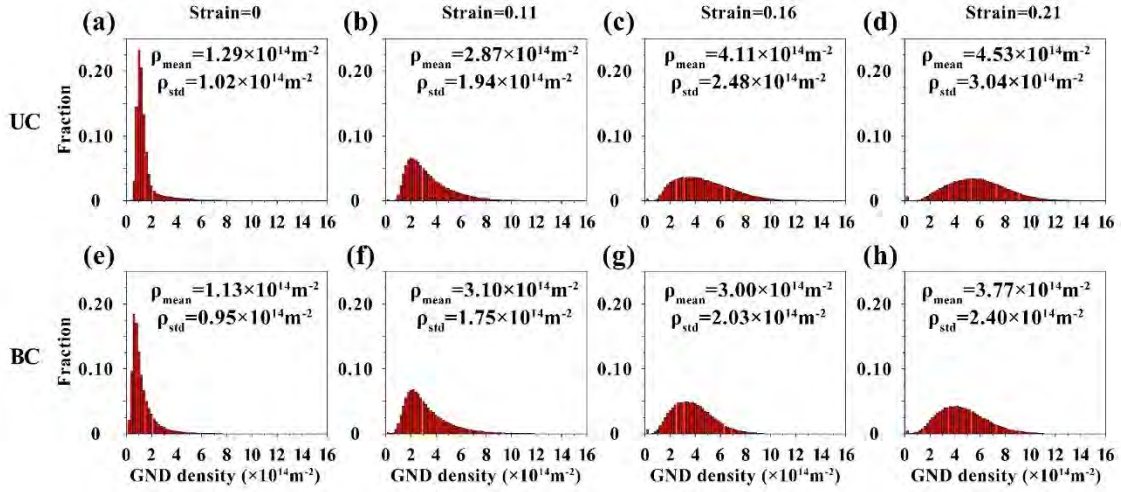


Fig. 14. Global GND density distribution on corresponding mapping results in Fig. 13 and (a-h) in this figure are related to (a-h) in Fig. 13. The mean value of GND density as well as the standard deviation are labeled in each histogram.

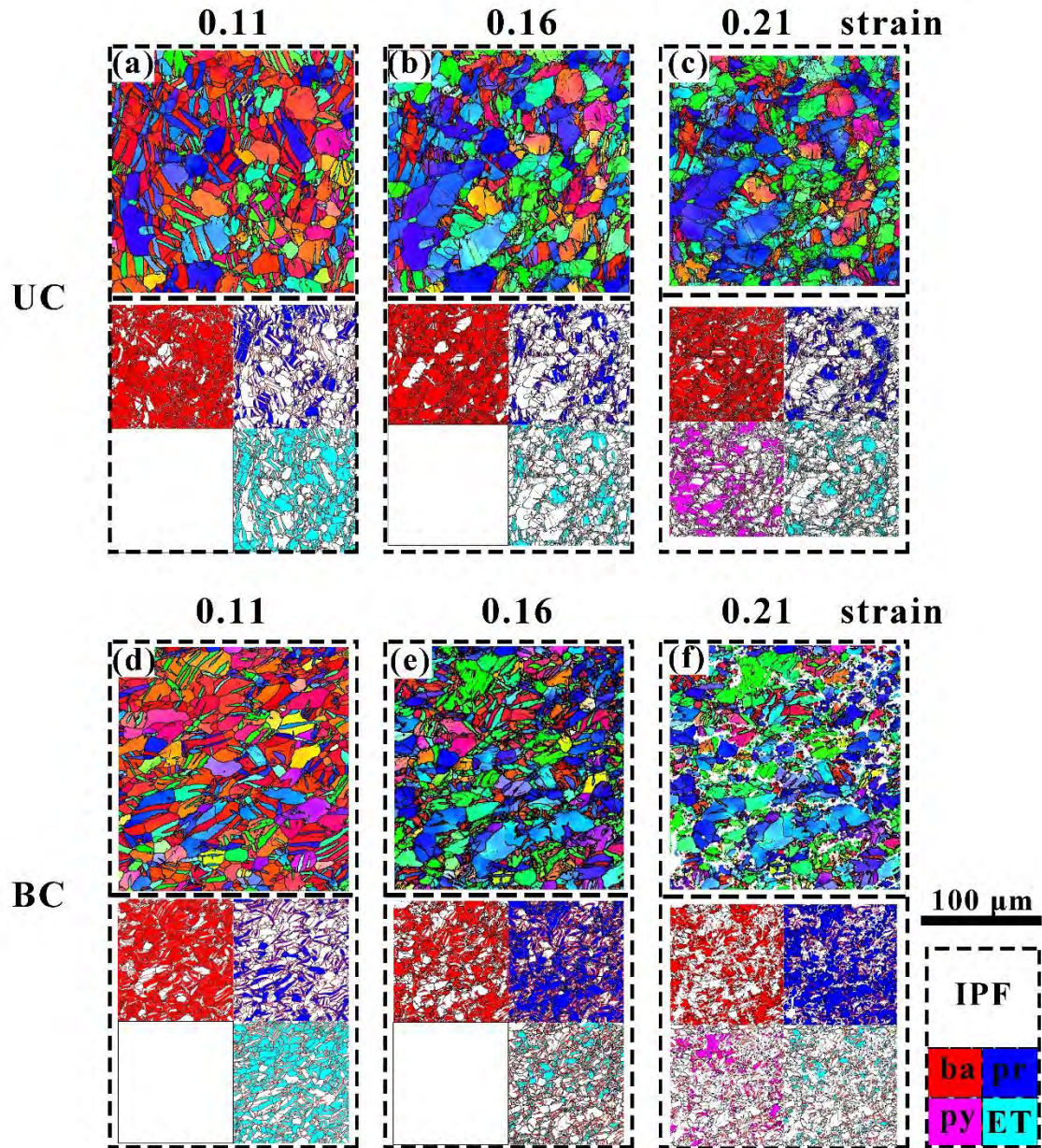


Fig. 15. The distribution of the grains, in which the corresponding deformation mechanism is possible to be activated in the samples under UC (a-c) and BC (d-f) at different strain level. The scalar bar is for the IPF.

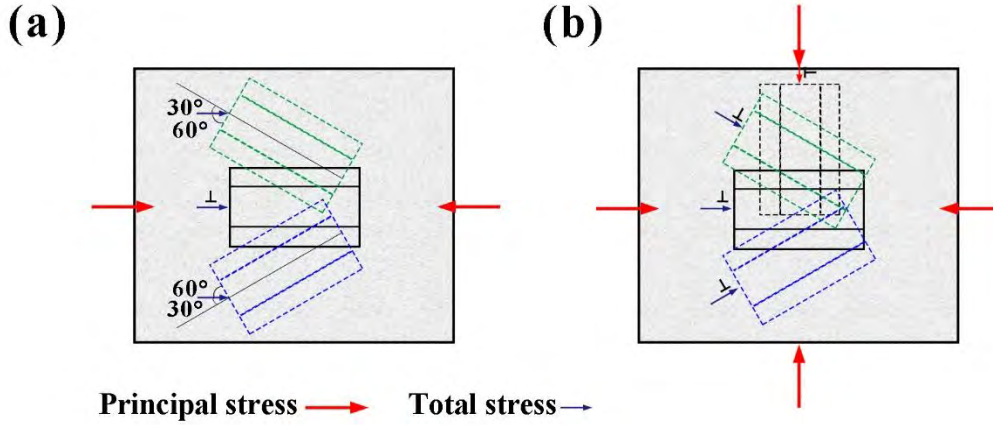


Fig. 16. The angle between the basal plane and the total stress in it: (a) under UC, (b) under BC. The thick or thin arrows indicate the directions of the macroscopic loads or the total stresses.

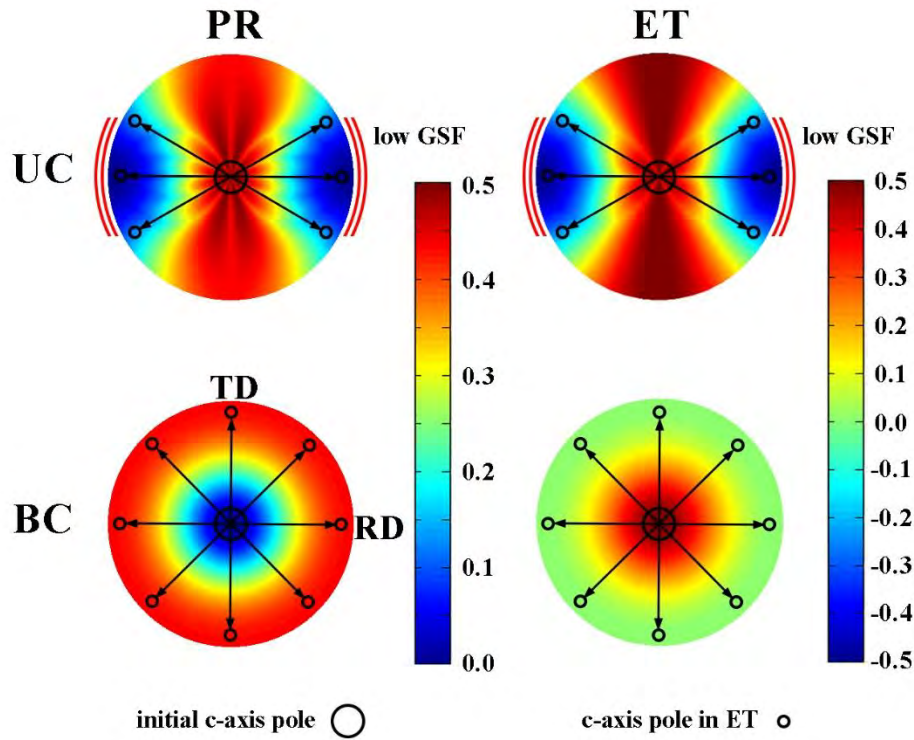


Fig. 17. Distribution of GSFs for prismatic slip and ET as a function of $\{0002\}$ PF. The load direction is along RD under UC. After ET under different stress states, the c-axis pole of the initial grain will tilt to several possible positions, as indicated in every PF.

Tab. 1. Chemical composition of the experimental materials (wt. %)

Alloy	Al	Zn	Mn	Mg
AZ31	2.89	1.26	0.27	Balance

Tab. 2. The statistical results of the grains or ET variants that obeying the Schmid law under UC and BC. The total numbers of the grains or ET variants in the measured regions are listed in the brackets.

	UC	BC
Obedient grain	96% (165)	88% (200)
Obedient variant	80% (504)	76% (503)

Tab. 3. Parameters used for VPSC-TDT simulation for AZ31 rolled sheets under UC and BC.

	τ_0 (MPa)	τ_1 (MPa)	θ_0 (MPa)	θ_1 (MPa)	A_1	A_2
Basal <a>	26	5	500	110		
Prismatic <a>	95	55	1000	130		
Pyramidal <a+c>	140	180	3500	70		
ET	38	0	0	0	0.25	0.9

Tab. 4. The calculated CRSS (MPa) used for the calculation of grain yield behavior at different strain levels.

	BA			PR			PY			ET		
	0.11	0.16	0.21	0.11	0.16	0.21	0.11	0.16	0.21	0.11	0.16	0.21
UC	36.5	41.9	46.9	95.0	95.2	96.6	140.0	148.2	160.8	38.0	38.0	38.0
BC	33.6	35.7	37.2	134.0	154.6	167.6	140.0	140.0	142.1	38.0	38.0	38.0

Tab. 5. The load value (MPa) and the equivalent stress strength used for the calculation of grain yield behavior at different strain levels.

	0.11			0.16			0.21		
	RD	TD	$\bar{\sigma}$	RD	TD	$\bar{\sigma}$	RD	TD	$\bar{\sigma}$
UC	-306	0	306	-390	0	-390	-397	0	397
BC	-273	-280	276	-332	-341	336	-388	-391	390

Credit authorship contribution statement:

Dabiao Xia: Writing - original draft, Investigation, Methodology, Conceptualization.

Junlei Zhang: Writing - review & editing, Investigation. Xiang Chen: Writing - review

& editing, Investigation. Guangsheng Huang: Writing - review & editing, Supervision,

Project administration, Conceptualization, Funding acquisition. Bin Jiang: Writing -

review & editing, Supervision, Project administration, Conceptualization, Funding

acquisition. Aitao Tang: Conceptualization, Methodology, Investigation. Sarkis

Gavras: Writing – review, Conceptualization. Yuanding Huang: Writing – review,

Methodology, Conceptualization. Norbert Hort: Methodology, Conceptualization.

Fusheng Pan: Conceptualization, Funding acquisition.